2019-03-01

Strain Path Effect on Austenite Transformation and Ductility in TBF 1180 Steel

Parker Kenneth Gibbs
Brigham Young University

BYU ScholarsArchive Citation

Gibbs, Parker Kenneth, "Strain Path Effect on Austenite Transformation and Ductility in TBF 1180 Steel" (2019). *All Theses and Dissertations*. 7127.
https://scholarsarchive.byu.edu/etd/7127

Strain Path Effect on Austenite Transformation

and Ductility in TBF 1180 Steel

Parker Kenneth Gibbs

A thesis submitted to the faculty of
Brigham Young University
in partial fulfillment of the requirements for the degree of

Master of Science

Michael P. Miles, Chair
Yuri Hovanski
Jason M. Weaver

School of Technology

Brigham Young University

ABSTRACT

Strain Path Effect on Austenite Transformation and
Ductility in TBF 1180 Steel

Parker Kenneth Gibbs
School of Technology, BYU
Master of Science

TBF 1180 steel was studied under various conditions focusing on the correlation of ductility and amount of retained austenite. Samples were prepared from sheet stock and then strained using limiting dome height tooling (LDH), a standard uniaxial test frame, and a tensile stage for use in an electron microscope. The steel was observed in plane, biaxial, and uniaxial strain to determine its effect on retained austenite transformation and ultimately, ductility. Retained austenite was observed using a scanning electron microscope (SEM) equipped with an electron backscatter detector (EBSD) to distinguish the different phases present. Initial austenite levels were around 5% by volume and was quickly reduced as the sample was strained. The biaxial samples were the slowest to transform, having about 2.5% austenite at .05 effective strain, which allowed the specimen to reach an effective strain of .3 with 1.1% austenite remaining. In contrast, the plane strain samples had the fastest rate of transformation having only 1.2% austenite at .05 effective strain and .7% austenite at a final effective strain of .18. Both forms of uniaxial, (*in-situ* and *ex-situ*), were near identical, as expected, and exhibited an austenite transformation curve between that of the plane and biaxial curves. The uniaxial austenite level at .05 strain was 2.1% and was able to reach about .15 strain with a final austenite percentage around 1%. It was concluded that the biaxial strain path had the greatest ductility due in part to its slower austenite transformation rate while plane and uniaxial strain paths were not as ductile with their faster austenite transformation rates.

ACKNOWLEDGEMENTS

I'd like to start by thanking Brigham Young University and all the professors whom I've had the benefit of learning from. If it weren't for them instilling a desire to learn in me, I wouldn't have continued my education through a master's program.

Of all my teachers, Dr. Michael Miles was especially pivotal for this research project. For every period of slow results, he was sure to keep pushing me until things picked up again. Despite my lack of knowledge on several points of research he was sure to continuously aim me in the right direction. In addition to Dr. Miles, Dr. David Fullwood was very helpful source of knowledge on the topic of material science. His expertise guaranteed that I always had a research question to answer. I would also like to thank Hannah Evanson for taking time out of her schedule to lend a helping hand for the project.

Going back further, my family deserves the most credit for keeping me on this path. I have two sisters and a brother that have helped in little ways with every step. My mother was always there to make sure I was doing alright while my dad provided encouragement and answers to some of my technical questions. Most of all, my loving wife deserves credit for supporting me day after day and allowing me to pursue my passions.

TABLE OF CONTENTS

LIST OF TABLES

LIST OF FIGURES

1   INTRODUCTION

1.1   Background

The primary goal of this research is to understand more fully and to characterize the microstructure and ductility of TBF 1180 steel by studying the transformation of austenite to martensite following various strain paths. The results of this study, along with results of other studies, will provide automotive manufacturers some of the required information to determine if TBF 1180 has enough ductility for forming, enough strength for safety requirements and is more cost effective than the current and other potential solutions for critical automotive body structures.

1.1.1   Advanced High Strength Steels

Advanced High Strength Steels (AHSS) are a classification of steels that are made by carefully controlling the cooling rate as the steels pass through the austenite phases at either the hot mill or the annealing furnace. AHSS are typically multiphase steels containing ferrite, martensite, bainite, and possibly austenite with multiple alloys possible producing a variety of material characteristics. The high tensile and yield strengths combined with the low relative weight have made various AHSS attractive to the automotive industry (Choi, 2009). AHSS typically have a tensile strength of over 600 MPa and a yield strength of 300 MPa, although many alloys have a tensile strength in excess of 1000 MPa. The list of common AHSS includes Duel Phase (DP), Transformation induced plasticity (TRIP), Martensitic, and Complex Phase (CP). Each alloy has

a specific set of characteristics that qualify it for the various structural requirements on a vehicle including energy absorption, fatigue, strength, stiffness and formability (Kuziak, 2008).

Currently, a hot-pressed boron high strength steel is used for the "B" pillar in many of General Motor's vehicles. This is a costly procedure and has been the subject of significant research to determine if there is a suitable replacement.

1.1.2 TRIP Steels

Transformation induced plasticity (TRIP) steels were created and introduced as a potential solution for the continuously changing automotive industry to meet the need of high strength, low weight materials. They provide excellent tensile strength above 700 MPa, with elongation in some cases above 70%, making them a great candidate to meet the demanding requirements for lightweighting the current generation of cars (Kwon, 2010, Shaw, 2001). What makes TRIP steels unique is their microstructure, and how it reacts to strain. The latest generation of these steels is composed of fine-grained ferrite, carbide free bainite, martensite, and retained austenite. It is the retained austenite that is the key to the TRIP effect because of its semi-stable state which transforms to a much harder martensite phase as it is strained (Grajcar, 2012).

This research is aimed at determining the correlation of the TBF 1180 alloy's strain path and strain level to its percentage of retained austenite so as to provide the automotive engineers with the information required to determine if TRIP steels have the ductility and strength to be formed at room temperature yet still meet the strength requirements of the car's design.

1.1.3 TBF Steels

Within the subset of TRIP assisted steels is the narrower classification of steel containing a bainitic ferrite matrix known as TBF steels. The process by which TBF steels are made is by hot

rolling or annealing after cold rolling, followed by austempering at a temperature within the bainite transformation range (Sugimoto, 2009). This process results in a unique grain structure containing retained austenite suitable for the TRIP effect. Due to the austenite formation and unique metallurgy, TBF steels can have fatigue limit and impact toughness values that are more than those found with other steels of similar strength (Sugimoto, 2009).

For the purposes of this study, it should be noted that a significant advantage of TBF steels is the formability which is a result of its uniform, fine grain structure. This allows the material to stretch without interference of microscopic stress concentration sites (Sugimoto, 2006). It is this formability that makes TBF steels such a promising candidate for stamped automotive structural members where energy absorption and strength are required.

1.1.4   Forming Limit Diagram

A forming limit diagram (FLD) is a tool used by designers that graphically represents the amount a material can be stretched before it begins to tear. The FLD is a plot of both major and minor stains for the various strain paths to illustrate the limits.

1.2   Hypotheses

The primary hypothesis that will guide this research on the effect of strain path on TRIP, and Q&P (as a comparison from prior work), steel ductility is the following:

The rate of retained austenite transformation will be strain path dependent and will also depend on microstructure details, especially the morphology of the retained austenite.

1.3 Delimitations

This scope of this research will include the study of the TBF 1180 TRIP steels with respect to its formability and microstructure. Comparisons will be made between TBF 1180 and Q & P 1180, where all the results on the latter were completed in a prior study.

1.4 Definitions of Terms

AHSS – Advanced High Strength Steel. Steels that have an ultimate tensile strength of 550 MPa or above are considered AHSS.

TBF 1180 – A TRIP steel with an ultimate strength of 1180 MPa or 171 ksi, containing both bainite and ferrite in the microstructure.

TRIP steel – Transformation induced plasticity Steel

RA – Retained Austenite

Q & P 1180 – A TRIP steel with an ultimate strength of 1180 MPa or 171 ksi.

DIC – Digital image correlation

EBSD – Electron backscatter diffraction

FLD – Forming Limit Diagram

FIB – Focused Ion Beam

SEM – Scanning electron microscope is a type of electron microscope that produces images of a sample by scanning it with a focused beam of electrons.

Wire EDM– Electrical Discharge Machining using a wire where electrons arc from a consumable wire to remove material and cut sheet metal.

UTS – Ultimate Tensile Strength, the capacity of a material to withstand loading in tension.

2 LITERATURE REVIEW

2.1 Introduction

Over the past several decades, automotive manufacturers have been pushed to create safer, more fuel-efficient cars. This drive is the result of a combination of consumer demands and government regulations. Although consumers are most concerned with fuel economy during an oil crisis, advancements in fuel economy have allowed manufacturers to create cars with more power and fewer emissions yet maintain or beat the fuel consumption of older, less powerful models (Turrentine and Kurani, 2007). To reach the ever-increasing corporate average fuel economy (CAFE) standard set by the government, manufacturers have resorted to using non-traditional materials to reduce weight and subsequently, increase fuel economy. There has been a shift from traditional steels to more advanced materials such as high strength steels, aluminum and composites to create cars that meet or exceed current safety standards while reducing weight (Choi, 2009).

2.2 Advanced High Strength Steels

Advanced High Strength Steels (AHSS) are a classification of steels that are made by carefully controlling the cooling rate as the steels pass through the austenite phases at either the hot mill or the annealing furnace. AHSS are typically multiphase steels containing ferrite, martensite, bainite, and possibly austenite with multiple alloys possible producing a variety of material characteristics. The high tensile and yield strengths combined with the low relative weight
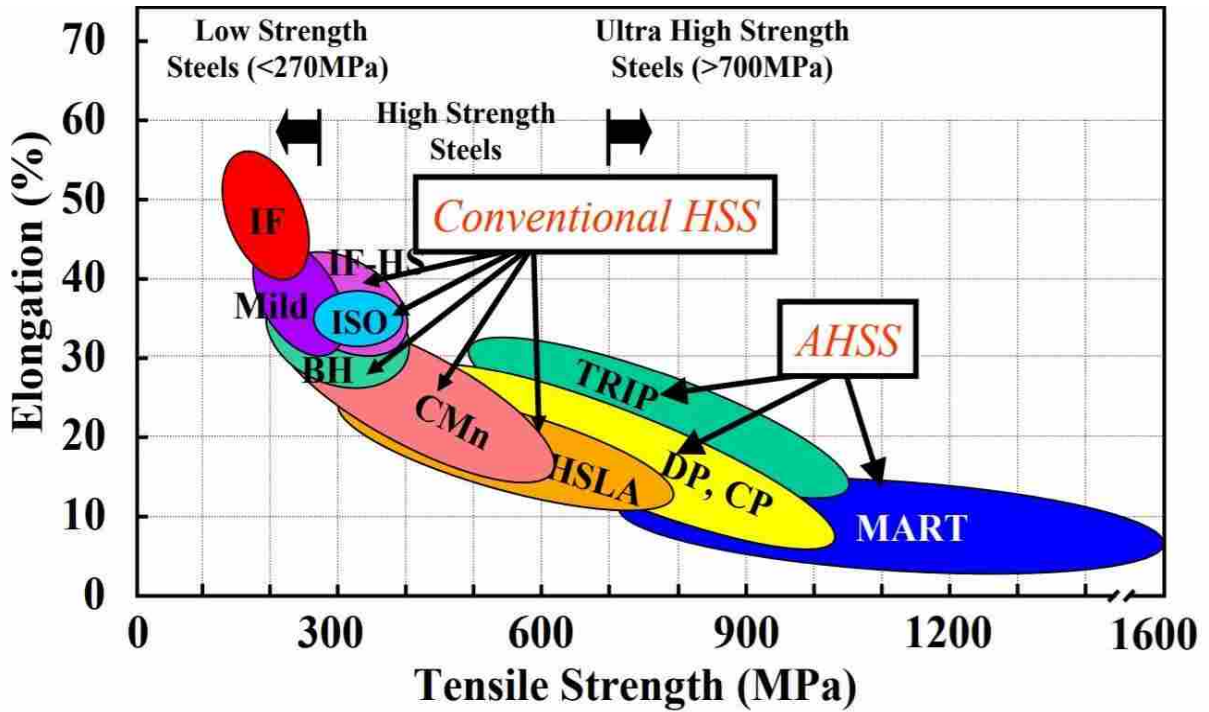
Figure 1-Total Elongation (%EL) vs. Ultimate Tensile Strength (UTS)

have made various AHSS attractive to the automotive industry (Choi, 2009). AHSS typically have a tensile strength of over 600 MPa and a yield strength of 300 MPa, although many alloys have a tensile strength of more than 1,000 MPa. The list of common AHSS includes duel phase (DP), transformation induced plasticity (TRIP), martensitic, and complex phase (CP). Each alloy has a specific set of characteristics that qualify it for the various structural requirements on a vehicle including energy absorption, fatigue, strength, stiffness and formability (Kuziak and Kawalla, 2008).

2.2.1   TRIP Steels

Transformation induced plasticity (TRIP) steels were created and introduced as a potential solution for the continuously changing automotive industry. They provide excellent tensile

strength above 700 MPa, with elongation in some cases above 70%, making them a great candidate to meet the demanding requirements for light-weighting the current generation of cars (Kwon, 2010, Shaw, 2001). What makes TRIP steels unique is their microstructure and how it reacts to strain. The latest generation of these steels are composed of fine-grained ferrite, carbide free bainite, martensite, and retained austenite. It is the retained austenite that is the key to the TRIP effect because of its semi-stable state which transforms to a much harder martensite phase as it is strained (Grajcar, 2012).

Previous research has uncovered many of the properties of TRIP steels in various conditions. For example, as the temperature of the steel decreases, the rate of austenite transformation decreases and subsequently allows for more strain before the austenite is depleted (Blonde, 2012). Other studies have gone into detail of how to analyze TRIP steels by using Scanning Electron Microscopes (SEM) and Electron Backscatter Diffraction (EBSD). Typically, TRIP steel specimens are polished and placed in an SEM equipped with an EBSD camera which allows for the fine distinction of face-centered phases (austenite) and body-centered phases (ferrite and martensite). Samples can be observed before, after, or during straining the specimen to determine the volume fraction of austenite at the various levels of strain (Blonde, 2012, Di Gioacchino and Fonseca, 2013). Using similar methods to these previous studies, this research is aimed at determining the correlation of the TBF 1180 alloy's strain path and strain level to its percentage of retained austenite.

2.2.2 TBF Steels

Within the subset of TRIP assisted steels is the narrower classification of steel containing a bainitic ferrite matrix known as TBF steels. The manufacturing process of this class of steels is similar to Quenched and Partitioned (Q&P) steels with the main difference being the austempering

temperature is much closer to the martensite start temperature for TBF steels (Sugimoto, 2007). The process by which TBF steels are made is by hot rolling or annealing after cold rolling, followed by austempering at a temperature within the bainite transformation range (Sugimoto, 2009). This process results in a unique grain structure containing retained austenite suitable for the TRIP effect. The retained austenite that is found in TBF steels forms more of a needle or film-like grain rather than a large "block" as is found in other TRIP steels as illustrated in figure 2 (Sugimoto, 2009). Due to the austenite formation and unique metallurgy, TBF steels can have fatigue limit and impact toughness values that are in excess of those found with other steels of similar strength (Sugimoto, 2009). TBF steel composition differs from other TRIP steels by containing a large amount silicon to prevent the formation of cementite. Despite this, alternatives to silicon are being researched because of the imperfections that the resulting silicon-oxides cause. Aluminum has been investigated but hasn't proven to be a worthwhile replacement due to the increased temperature required to austenitize the material. Niobium has shown promise as an alloying element to prevent the formation of cementite while refining the grain structure and increasing the amount of retained austenite (Hausmann, 2013). The current, typical composition for TBF 1180 can be observed below in table 1 (Hausmann, 2013).
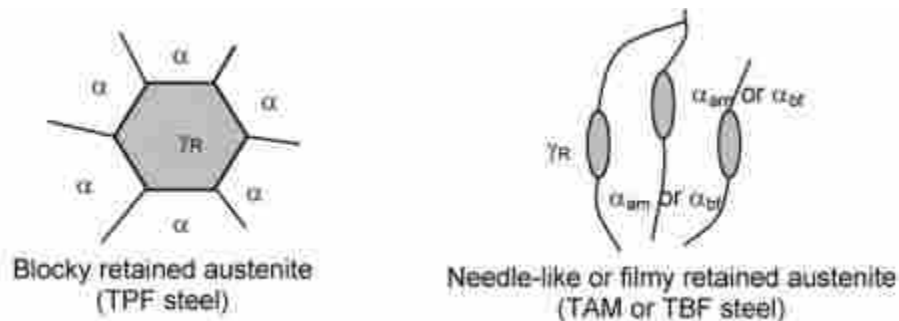

Figure 2-Representation of the Different Types of Austenite Formation

Table 1-Primary Composition for a Typical TBF 1180 Steel

C	Si	Mn	Nb	Al	N
.2	1.5	1.5-2.5	<.05	<.05	<.006

For this study, it should be noted that a significant advantage of TBF steels is the formability which is a result of its uniform, fine grain structure. This allows the material to stretch without interference of microscopic stress concentration sites (Sugimoto, 2006). It is this formability that makes TBF steels such a promising candidate for stamped automotive structural members where energy absorption and strength are required.

2.3   Plastic Strain Mapping with Digital Image Correlation

Digital Image Correlation (DIC) is a method of using computer software to track the movement of patterns on a surface and relate it to the amount of strain an object undergoes in a three-dimensional space. This is a common method to ensure accurate measurements of a material's plastic strain on both a microscopic and macroscopic level and has been used in similar studies where movement of metallic structures were observed (Di Gioacchino and Fonseca, 2013) . On the macroscopic level, paint is applied in a fine mist to provide a randomized speckled pattern which is then tracked by a pair of high-resolution cameras linked to computer with software which translates the images to a map of the deformed material. Microscopically, images are captured by the forward scatter detector (FSD) which is part of the EBSD equipment inside of the microscope. The FSD provides a high-quality image of the steel's topography which allows for DIC processing without the use of an etchant to provide contrast. The DIC software can then track the movement of specific pixels through the progressing images. In both cases, the software can correlate the movement of points to the amount of strain, resulting in a highly accurate measurement.

2.4   Forming Limit Diagram

A forming limit diagram (FLD) is a tool used by designers that graphically represents the amount a material can be stretched before it begins to tear. A feature of the FLD is the plot of both major and minor strains which allow the representation of the different strain paths (plane, uniaxial, and biaxial) (Moshksar and Mansorzadeh, 2003). The point at which a sheet can be stretched no more is referred to as the limit strain and is typically determined by a combination of experimentation and mathematical models. It has been found that FLD models mathematically derived specifically for TRIP steels have not been found to be coincident with experimental results (Bleck, 1998). Because of this, TRIP steels require an experimentally derived FLD for reference until an adequate mathematical model has been developed.

3 RESEARCH METHODOLOGY

3.1 Sample Prep and Polishing Micro-Tensile Test Specimens

Several sheets of TBF 1180 were obtained from General Motors and prepared for testing. All samples were cut from the sheet using either a wire-EDM or water jet for precise dimensions and to prevent any transformation of the austenite which would occur with less delicate processes. Samples that were strained on a dome press or on an Instron machine had large dog-bone shapes cut out using the water jet. The geometry for these samples was created using the guidelines of ASTM E8 for flat sheet specimens. Samples to be used on the small tension stage for use in a microscope were cut into small dog-bone shapes using a wire EDM. Samples strained on the larger machines had smaller .375" square samples cut out from them using the wire-EDM to be examined separately.

All samples prepared for microscope analysis were polished. The small dog bone samples and cutouts of larger samples were mounted to metal pucks to ensure even polishing as seen in figure 4 (Cramer, 2017). All samples were abraded using silicon carbide abrasive discs of various grits including 400, 600, 800, 1200, and 1200 fine. Each disc was used sequentially working with two sheets of each grit and the sample rotated 90 degrees after each disc to ensure an even polish. The final thickness of the *in-situ* samples needed to be 0.3-0.4 mm to avoid exceeding the 800N limit of the microscope tension stage which required some samples to be ground with multiple sheets of 120 grit paper. Once to thickness, the samples were removed and re-mounted so that the opposite side could be polished with the finer abrasives without the potential of austenite

transformation caused by the aggressive material removal. Dimensions of the samples can be found in figures 3 and 5.
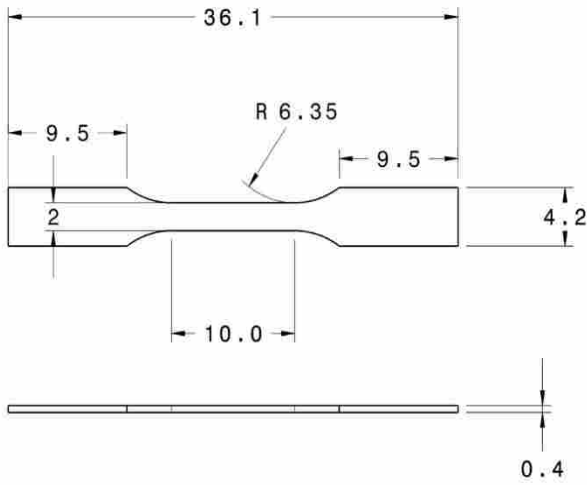

Figure 3-Dimensions of Dog Bone Micro-Tensile
Test Specimens in mm

Figure 4-Micro-Tensile Specimens
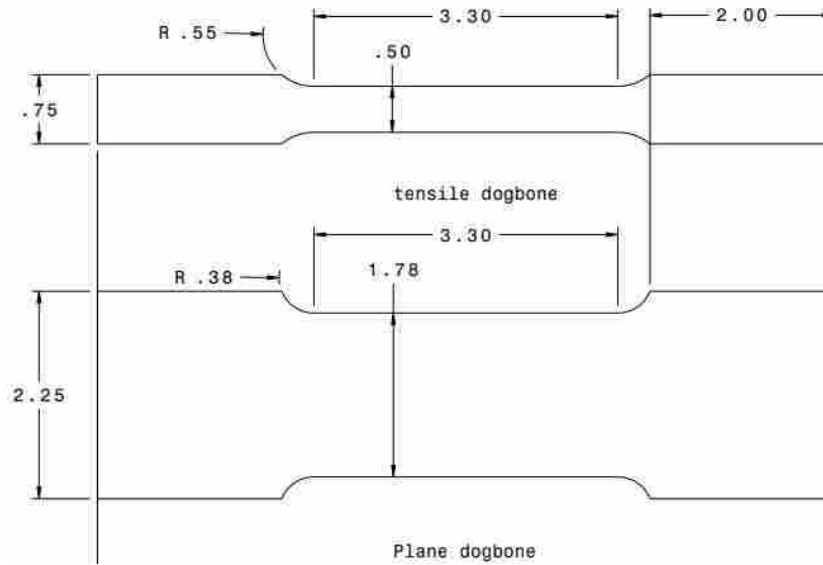Mounted on a Steel Puck

Figure 5-Uniaxial and Plane Strain Sample Geometry in Inches

The samples were then removed from the puck and electro polished using a freshly prepared electrolyte with a composition of 25 ml per-chloric acid, 75 ml butanol and 125 ml methanol. The solution was chilled to 10 °C by submerging the vessel in ice water as seen in figure 6. A sacrificial metal plate acting as the cathode was placed in the solution and the power supply was set to 20 volts. The sample, acting as the anode, was then submerged in the solution for 18 seconds at which point the power supply was switched off. The sample was then removed and rinsed with ethanol and dried with compressed air to prevent residue. Following the polishing, all samples were organized and stored under vacuum to prevent contamination. Powder free gloves were worn while loading or unloading the samples into the microscope to maintain the cleanliness of the samples.

Figure 6-Preparing the Electrolytic Solution for Sample Polishing

3.2   Marking Samples

For the initial *in situ* tests, the mini dog bone samples were marked with microscopic fiducials to ensure the same sites were being observed across the various strain levels. The fiducials were created by a FEI Helios Nanolab 600 microscope equipped with a focused ion beam (FIB) which can mill away the material and create the required patterns. The settings used were 2.6 nA beam current and 30 kv accelerating voltage with a 52-degree tilt on the sample. The fiducials were about 5-10 microns wide and tall and 0.7 microns deep as observed in figure 7. The overall pattern can be seen in figure 8 with the width being 2 mm and the height being 1 mm for the entire pattern (Cramer, 2017). Later *in situ* test were performed without fiducials due to the discovery
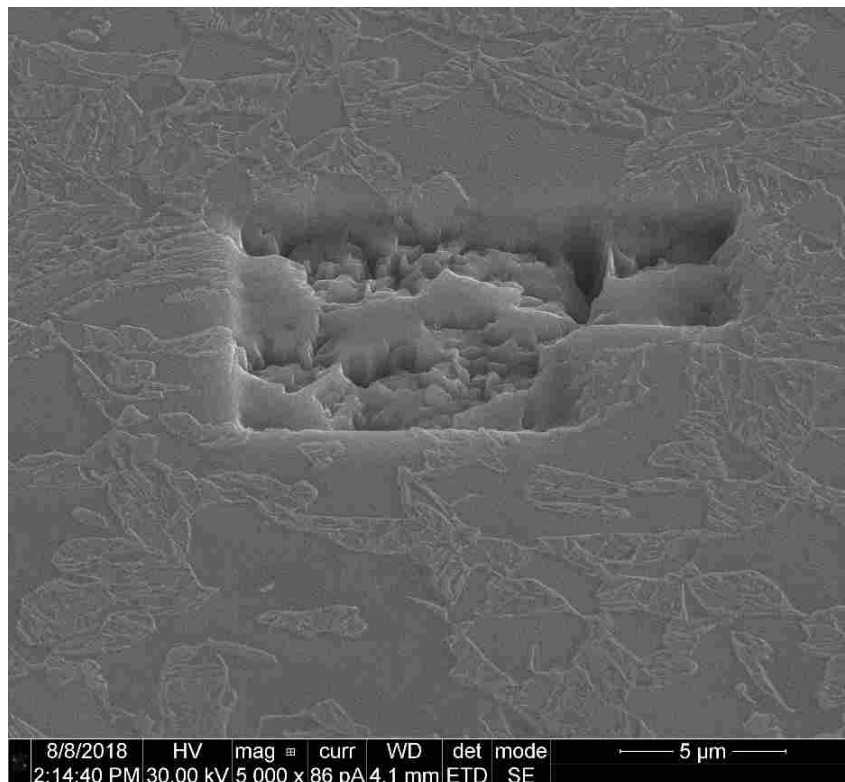

Figure 7-SEM Image of Ion Milled Area of Sample

that the FIB milling causes localized austenite transformation (Basa, 2014, Cramer, 2017). Scans were then aligned using recorded microscope coordinates and natural features on the sample surface which proved to be effective without causing unwanted austenite transformation.
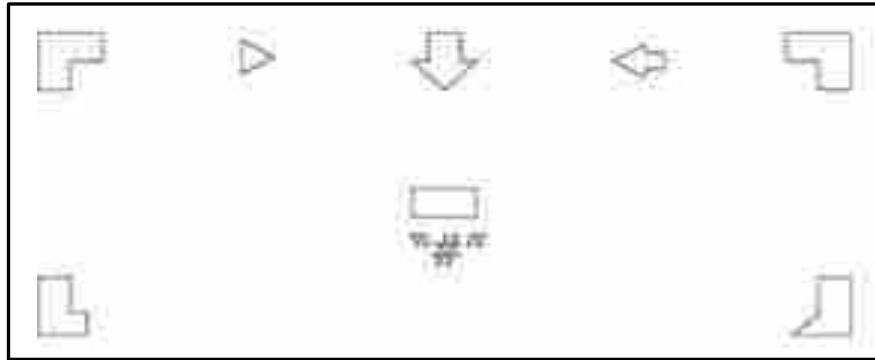

Figure 8-Fibbed Array Pattern with "#" Replaced with Sample Number

3.3 EBSD and Images of Micro-Tensile Test Specimens

The unstrained, small dog-bone samples were loaded into the microscope stage and pulled. Scans were taken at multiple locations at zero percent strain, followed by straining the sample in 0.2-millimeter increments. It is the nature of electron microscopes to deposit carbon on the sample which, due to the time required to scan an area multiple times, yielded some scans unusable. Samples were strained until failure or the quality of the scans was too poor to continue gathering data from. The microscope used was a FEI Apreo scanning electron microscope (SEM) equipped with an EDAX EBSD camera. The settings used were a 60-degree tilt angle with a 10-degree angle built into the stage, 20 kv accelerating voltage, 1.6 nA beam current, 0.08 micron step size, 17.5 x 17.5 micron scan size, and a working distance between 17 and 20 mm. The software used to analyze the EBSD patterns was OIM Analysis 7.

15

Retained austenite volume percentage was recorded for each sample and associated with the level of strain and the type of strain applied. From this data, a forming limit diagram was created, providing valuable information to resolve the hypothesis.

Figure 9-Micro Tensile Specimen Mounted in the In-situ Stage

Figure 10-Sandia Design In-situ Stage

Figure 11-Image of the Tensile Stage in the Microscope with the EBSD Camera in Place

3.3.1   EBSD Data Cleanup

Varying success with polishing, contamination and natural variations in material topology created static like noise in the EBSD scan images which necessitated a method of screening data. Without any data cleanup, the software reports this static as austenite, creating an artificially high percentage of retained austenite.

Several cleanup methods were examined to determine the one which would result in the most accurate report of austenite and ferrite percentages. The chosen method began by removing all points of data that had a confidence index of less than .1, meaning the software was not very certain of its interpretation of phase. Then, the points were cleaned by correlating an individual data point's orientation with the orientation of the neighboring points. This changed individual points to match its neighbors if surrounded by enough of a single orientation with a confidence index of greater than .1. Some austenite was reported as noise and as a result, was removed by later cleanup methods. To prevent this, the data for austenite was processed using a similar method but with neighboring phase rather than orientation, changing data points if enough of the surrounding points were of a single phase and interpreted with a high enough confidence index. Finally, all data was then cleaned by standardizing the confidence index within all grains larger than 3 points. It is important to note that this standardization did not change any interpretation of phase but rather created a more usable image. Following the cleanup, the total fraction of austenite was reported rather than the partition fraction due to the inaccurate values reported as the image quality degraded.

The OIM analysis software is unable to distinguish between ferrite and martensite. The significance of this is that martensite, transformed austenite, and ferrite are all interpreted the same and shown in green in all phase-map images. Austenite is shown in red.
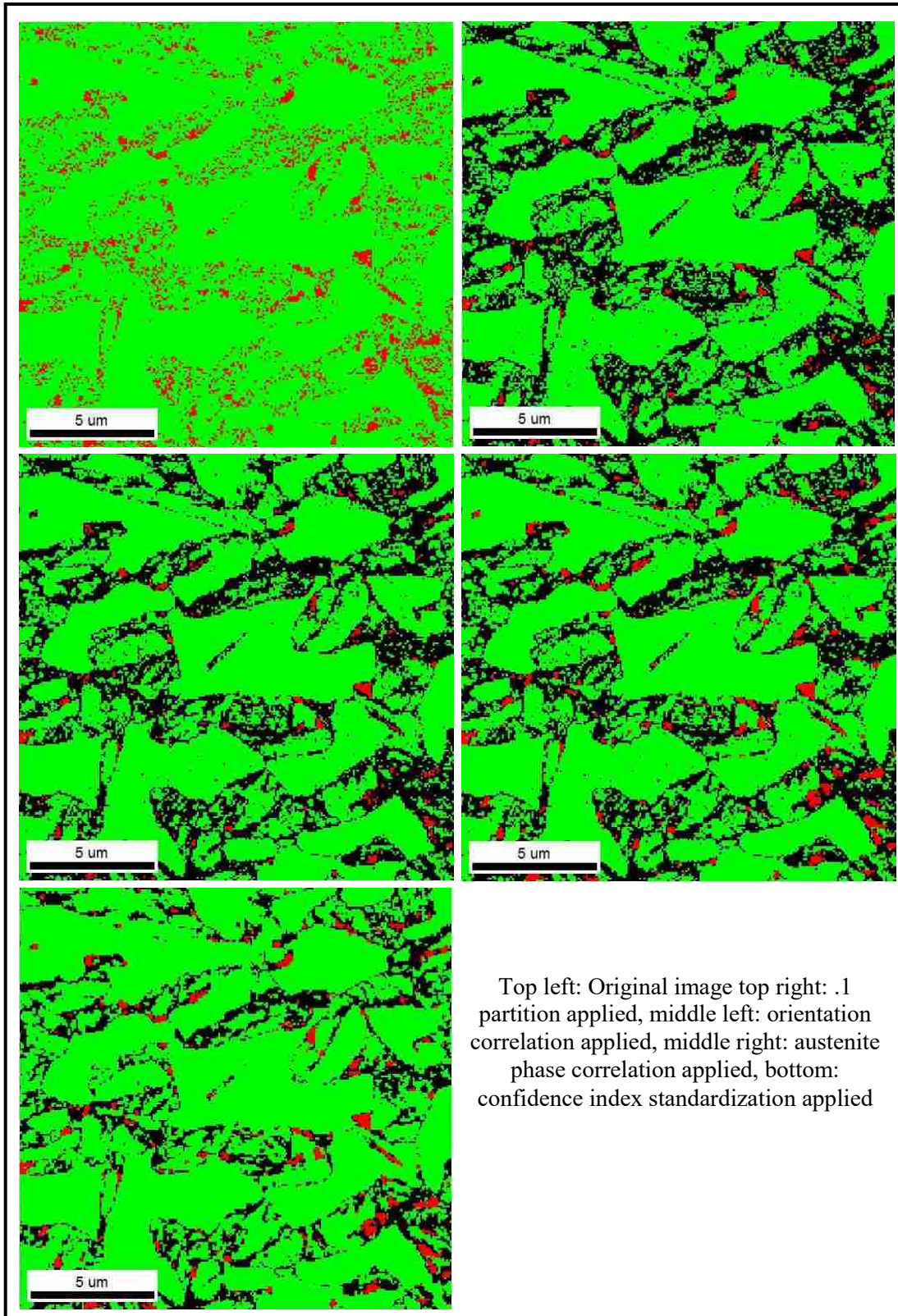
Top left: Original image top right: .1 partition applied, middle left: orientation correlation applied, middle right: austenite phase correlation applied, bottom: confidence index standardization applied

Figure 12-4 Step Image Cleanup

18

3.4   **DIC Image Processing of Micro-Tensile Test Specimens**

The software that was used to process the DIC images was GOM Correlate due to its ease of use and compatibility with the cameras used for the macroscopic DIC images. This software has the capability to translate the motion of individual pixels across multiple sequential images and correlate it to a three-dimensional map of a material's strain. This software provided the capability to pinpoint the exact major and minor strain which was crucial for identifying regions of plane strain and determining the effective strain at the site of sample removal (Systems, 2011).

3.5   **Macroscopic Samples and Equipment**

The experiments for plane and biaxial strain were performed on an Interlaken hydraulic press with a clamp load of 334 kN and a maximum punch load of 223 kN. The tooling included clamps with small lock beads to restrain the blank while preventing it from tearing and a dome punch with a 100 mm diameter. The macroscopic uniaxial strain was performed on an Instron test frame with 50kN load cell. A random pattern was applied to the blank samples by lightly spraying black paint over a white painted surface to create a fine speckle which allows the DIC cameras to track motion. The system used was an Aramis Digital Image Correlation (DIC) dual camera system equipped with 52 mm lenses.

Several samples were strained to failure for all strain paths followed by samples strained to 25%, 50%, and 75% of the averaged failure displacement amount. Four smaller, .375" samples were then cut out and polished following the method outlined above before being mounted on a microscope sample holder to be scanned using EBSD.

Figure 13-Tooling Used for Plane Strain and Biaxial Tension Experiments

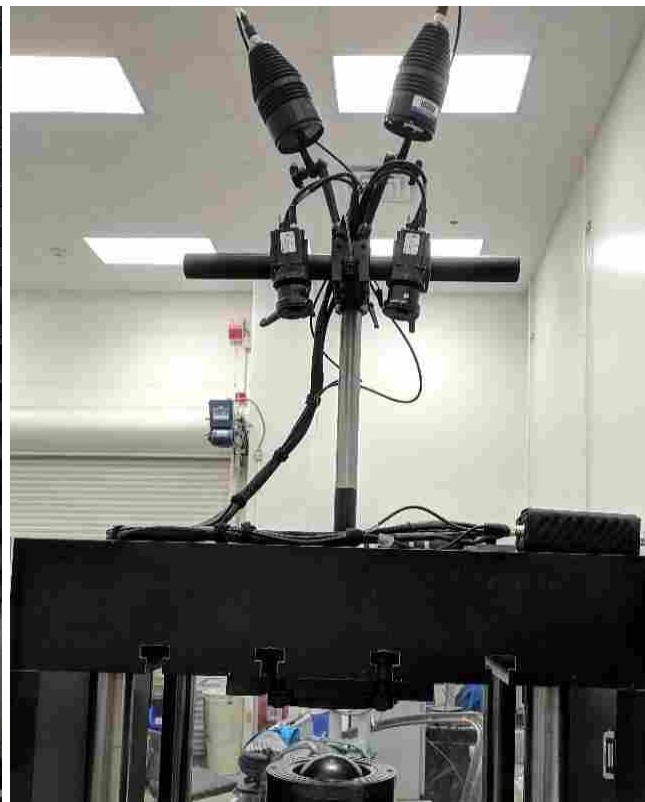Figure 14-Instron Test Frame for Uniaxial Testing

Figure 15-DIC Camera and Lighting Fixture

4 RESEARCH RESULTS AND DISCUSSION

4.1 Individual Strain Path data

Upon observation of various strained and unstrained samples of TBF 1180, it can be concluded that austenite transforms as the sample is strained and that the rate of transformation is correlated with the strain path. With all the effective strain levels plotted with their respective austenite volume percentages, this correlation becomes clear. The averaged data for each strain path can been seen below in figure 16. The biaxial samples transformed austenite at a much
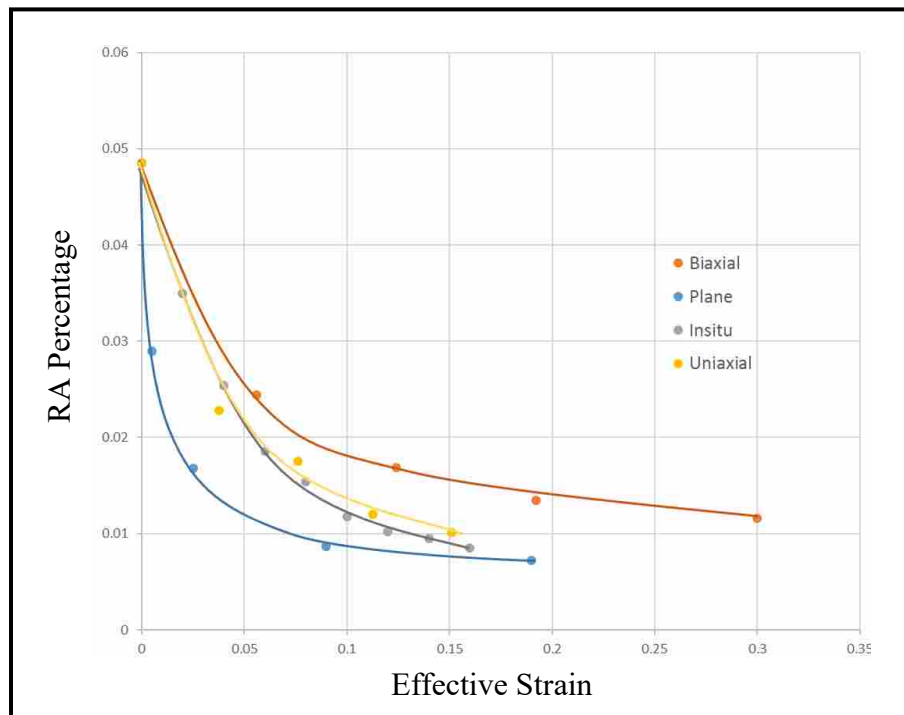
Figure 16-RA Percentage as a Function of Effective Strain

slower rate when compared to the uniaxial and plane samples, possibly explaining the higher effective strain reached before failure. Uniaxial tension results proved to be similar between *in-situ* and *ex-situ* samples, as expected. Thinning strains were calculated for each path and plotted below in figure 17. Further results for individual strain paths will be discussed below.
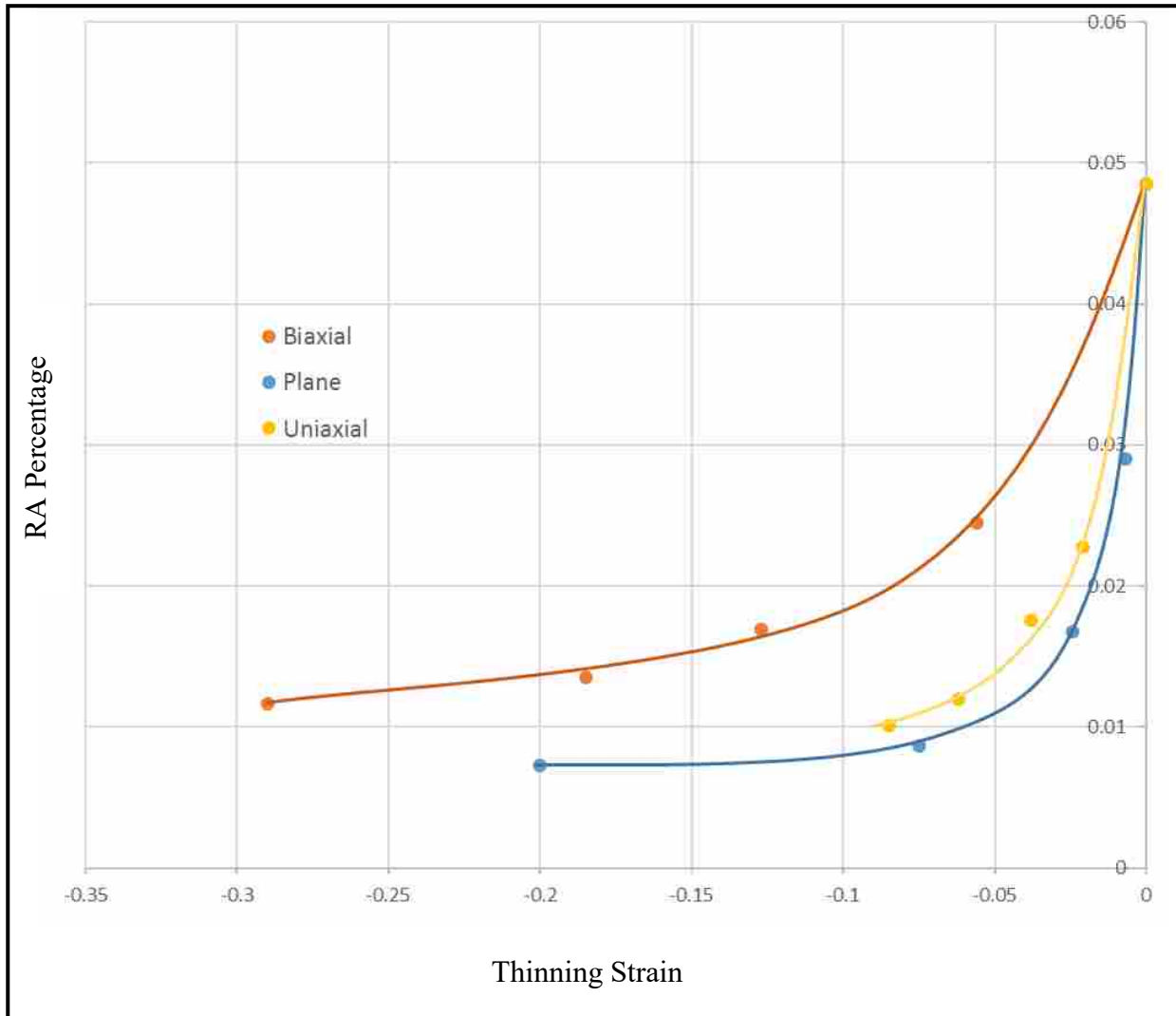

Figure 17-RA Percentage as a Function of Thinning Strain

4.1.1 Biaxial Strain Path

Individual data points comparing the true major and minor strains obtained from DIC software were potted in figure 18, showing that the sample was in true biaxial strain at the site of sample removal.
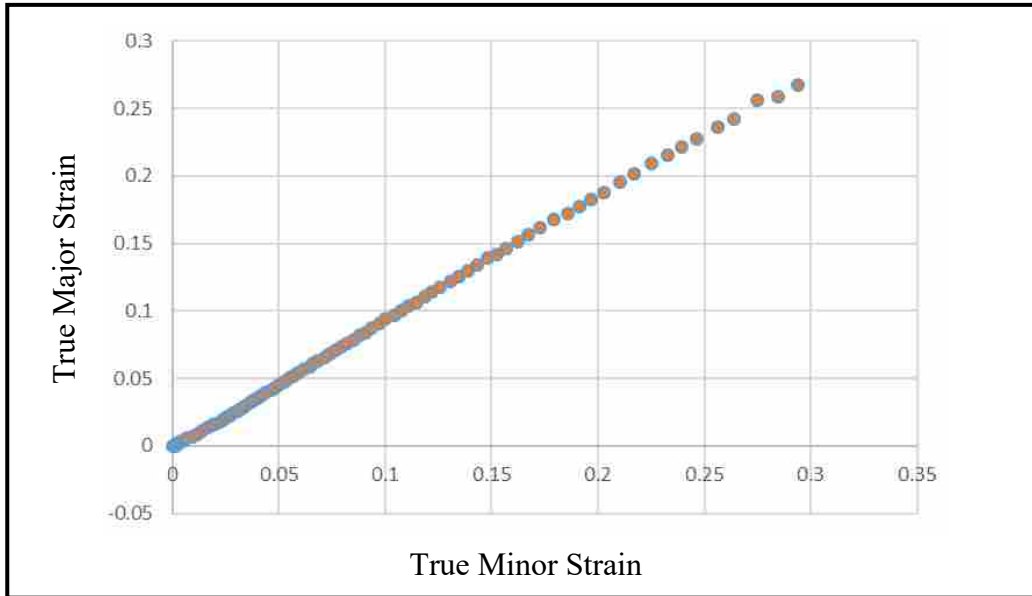

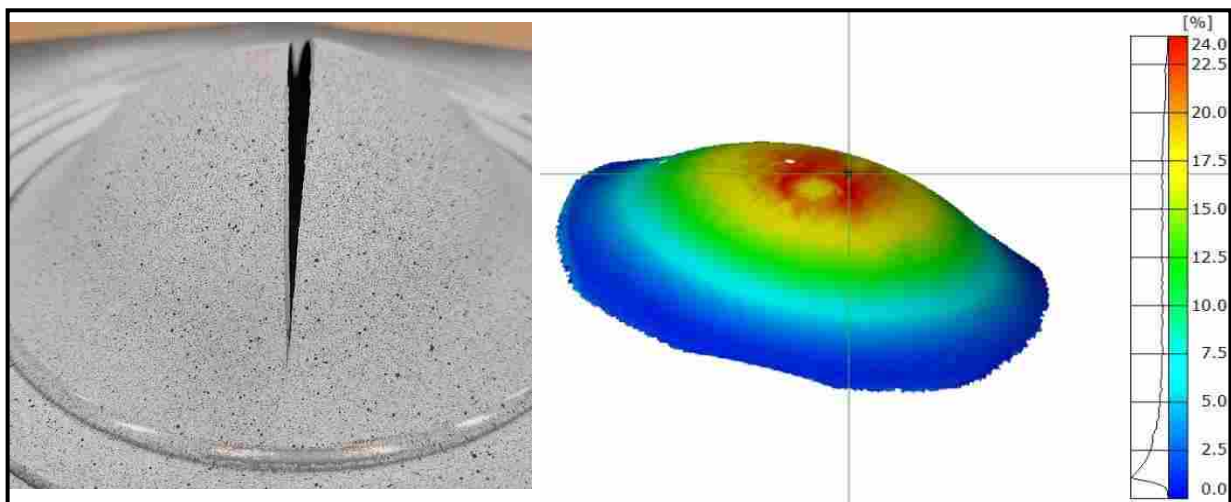Figure 18-Strain Path from DIC Measurements for the Biaxial Sample

Figure 19-Biaxial Sample Removal Site and DIC Image Displaying Major Strain
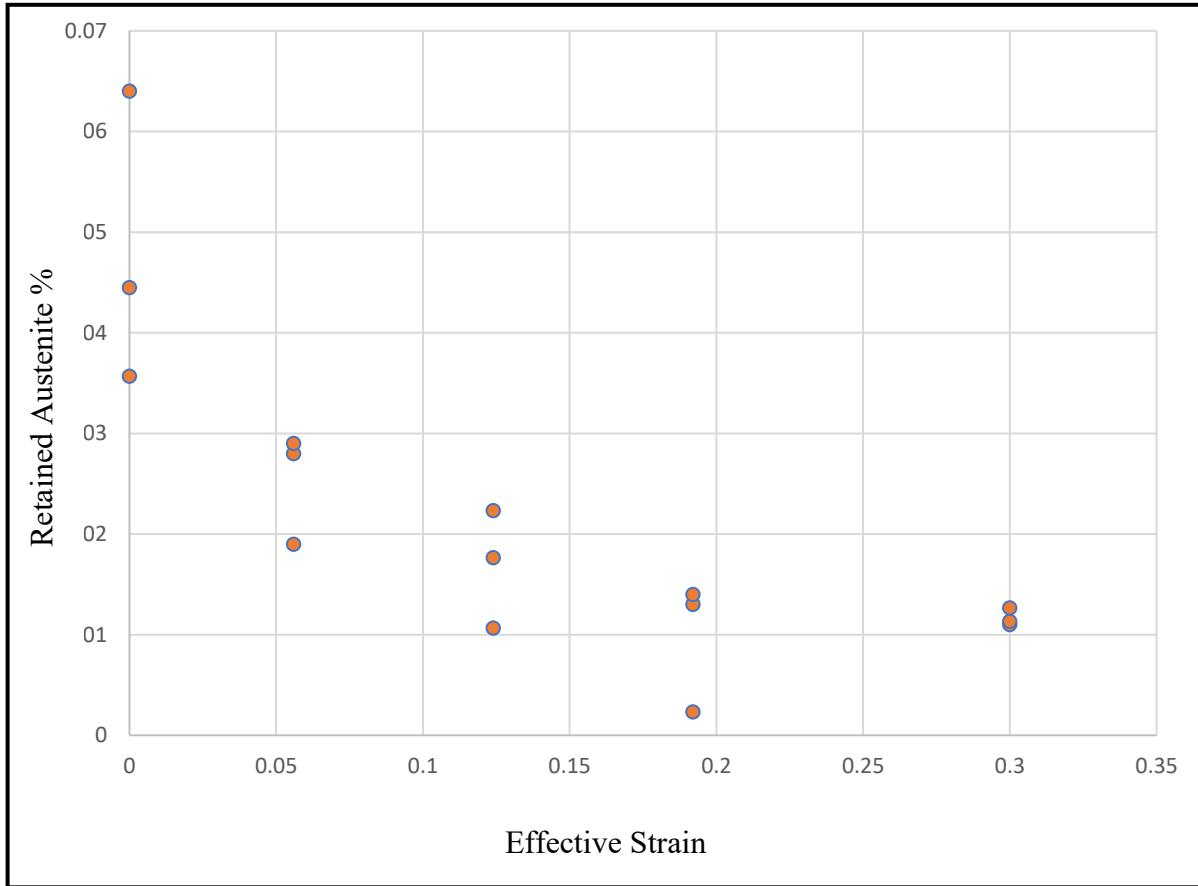
Figure 20-Percent RA as a Function of Effective Strain for Biaxial Strain

Figure 20, above, is a plot of the retained austenite percentages for each strain increment. Each point represents the averaged percentage from multiple scans of the same orientation. Although the exact numbers varied from scan to scan, the downward trend of austenite percentage remains consistent. Of all the strain paths, biaxial had the smoothest curve meaning that the rate of austenite transformation was more evenly spread across the straining of the sample. The scans of failed samples yielded an austenite percentage of just above 1% which is the highest of the three strain paths.

4.1.2 Plane Strain Path

Individual data points of the failed plane strain sample can be seen below in Figure 21. It should be noted that although the sample experienced some strains in the minor direction, the amount of minor strain experienced by the sample is relatively small compared to the major strain.
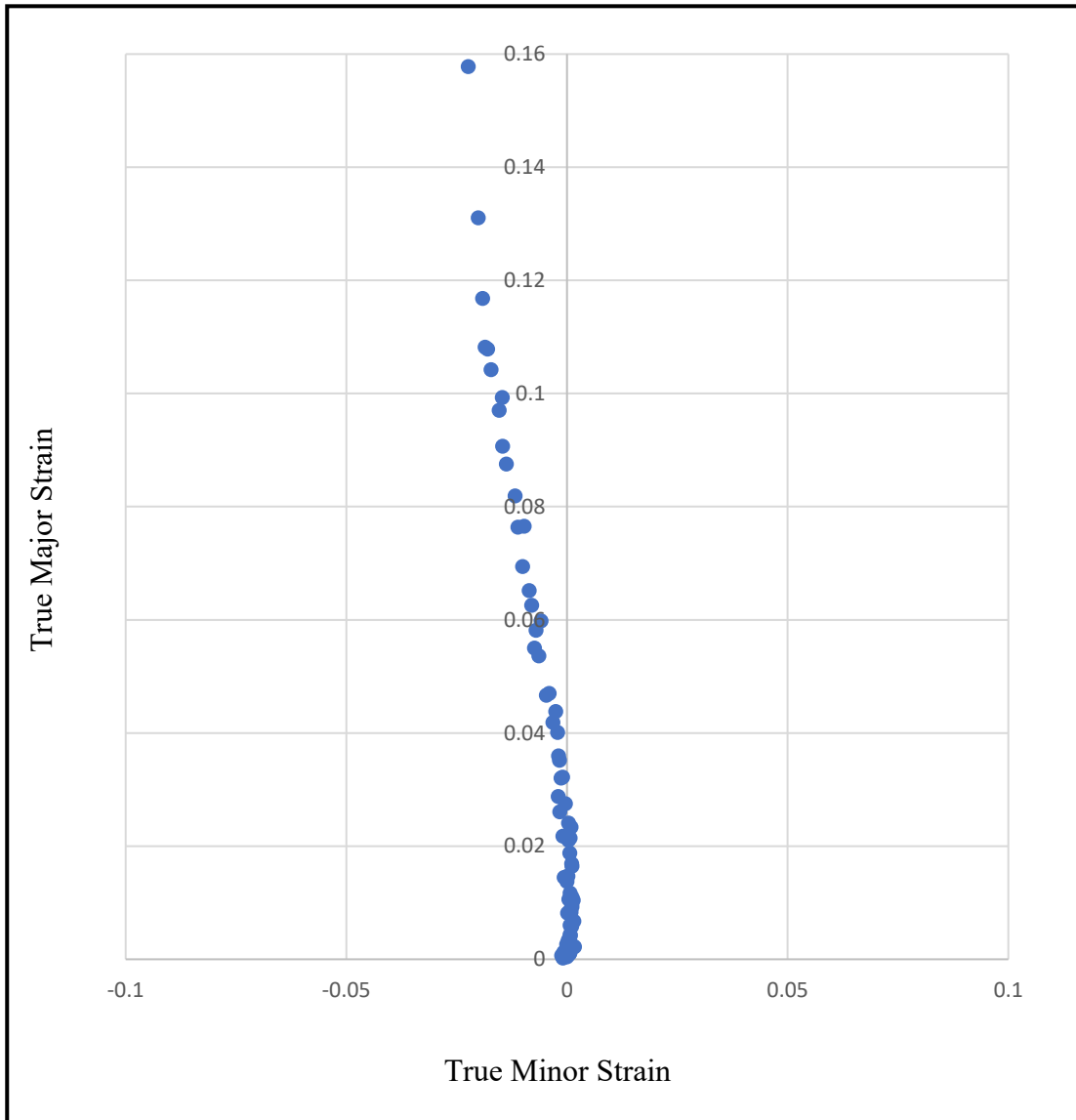

Figure 21-Strain Path from DIC Measurements for Plane Strain
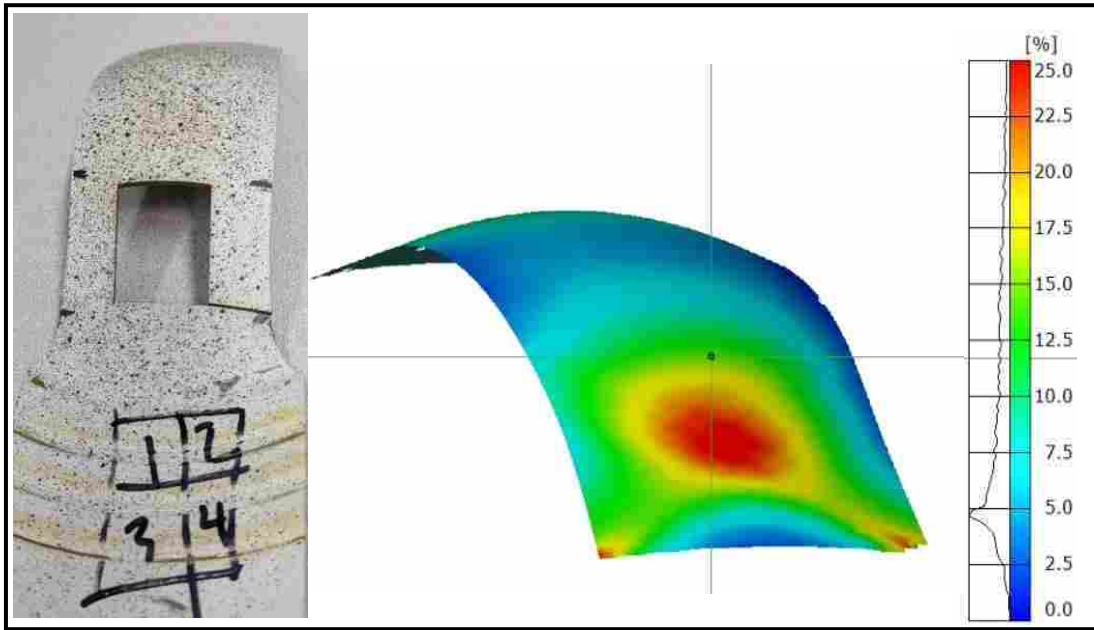
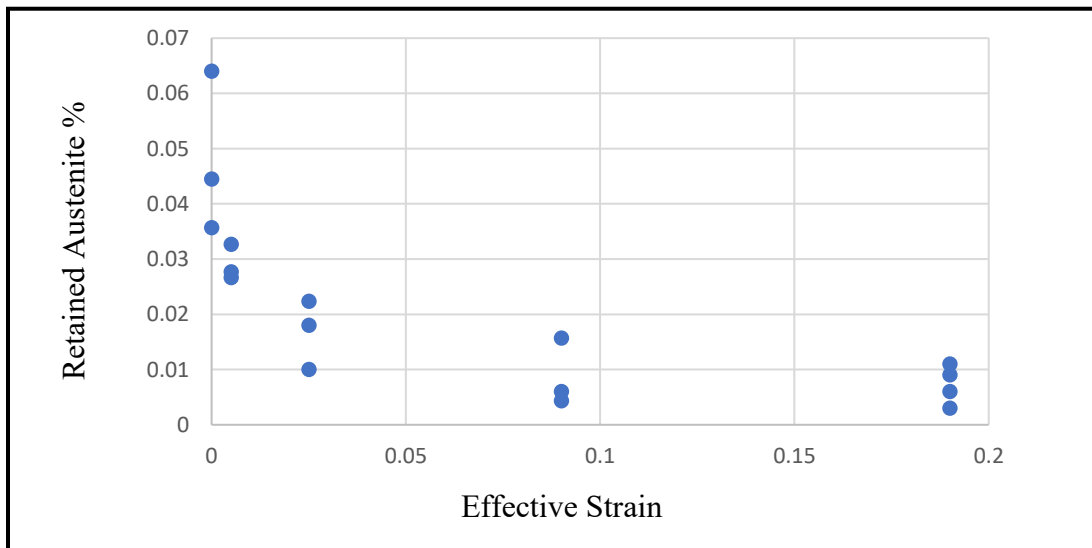Figure 22-Plane Sample Removal Site and DIC Image Displaying Major Strain

Figure 23- Percent RA as a Function of Effective Strain for Plane Strain

The association of effective strain and % retained austenite can be seen above in Figure 23.

Interestingly, the plane strain path displayed the sharpest curve, with most of the austenite

transforming early in the path. The curve drops sharply, but then quickly tapers off before the .05 effective strain mark. In contrast to the biaxial path, the austenite in this sample reached a lower overall percentage which could possibly be attributed to the high rate of transformation early in the path.

4.1.3   Uniaxial Strain Path

The collection of data for the uniaxial strain path includes both results from the samples strained macroscopically on the Instron test frame as well as the smaller samples strained *in-situ* with the microscope and tensile stage. Data points for all values can be found below in figure 24.
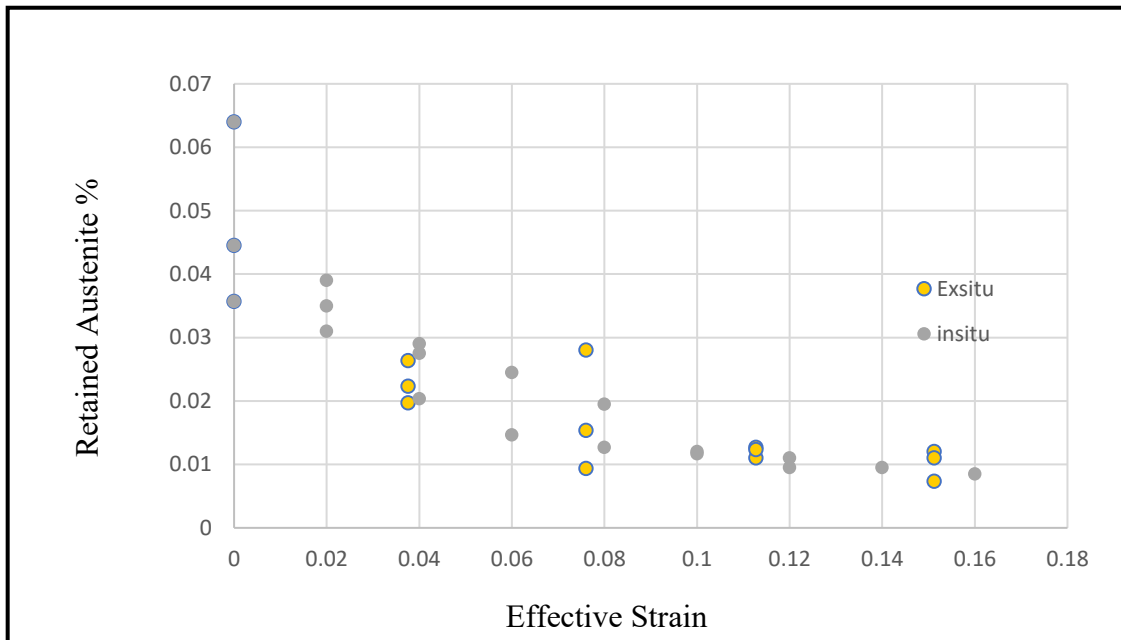

Figure 24- Percent RA as a Function of Effective Strain for Uniaxial Strain

This data confirms that steel behaves similarly for both *in-situ* and *ex-situ* uniaxial tension. The trend for this strain path falls between those for biaxial and plane strain paths. The rate of

austenite transformation isn't as gradual as the biaxial path yet isn't as fast as the plane strain path. Similarly, the average remaining austenite at failure is less than biaxial samples but more than plane strain samples.
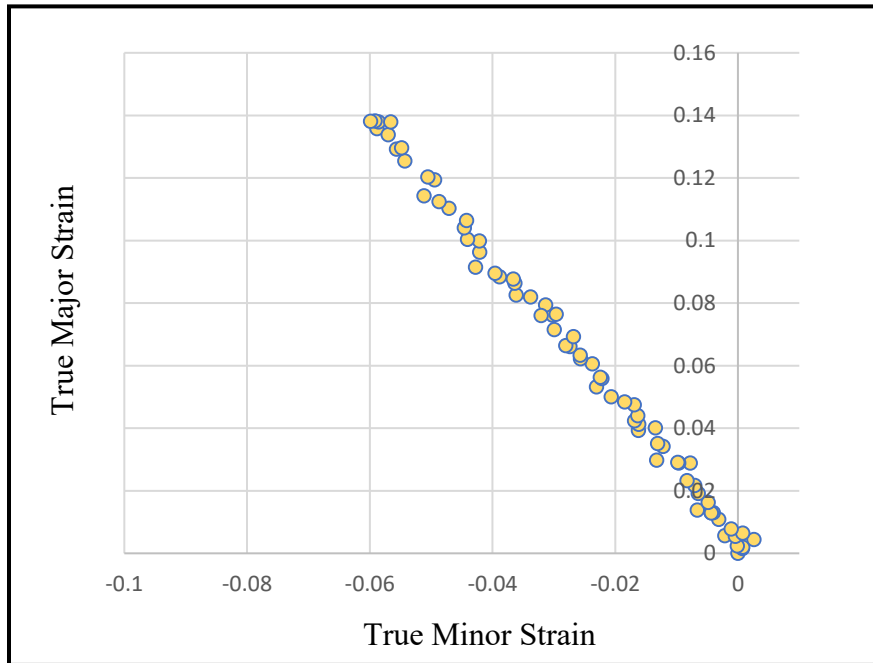

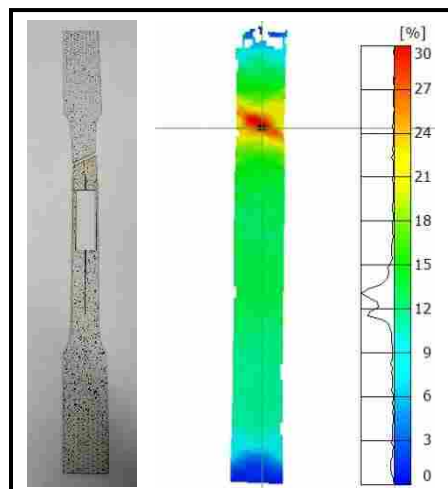Figure 25-Strain Path from DIC Measurements for Uniaxial Strain

Figure 26-Uniaxial Sample Removal Site and DIC Image Displaying Major Strain

DIC data obtained during the tension tests revealed that the major strain at any given point is roughly double what the minor strain is at that same point as displayed in figure 25, which is to be expected for uniaxial loading.

The phase maps, below in figures 27-33, reveal the grain structure and austenite transformation of a single location as a sample is strained. The green areas represent ferrite, martensite and transformed austenite while the red areas are exclusively austenite. Most of the austenite is depleted throughout the transformation, starting with 5.4% austenite at 0% strain, decreasing to 1.3% at 12% strain. This sample failed at 12% strain although the other samples were pulled in excess of 16% strain. However, most of the scans past the 12% strain level were of poor quality, allowing only data from a few samples to be included in the calculations at higher strains
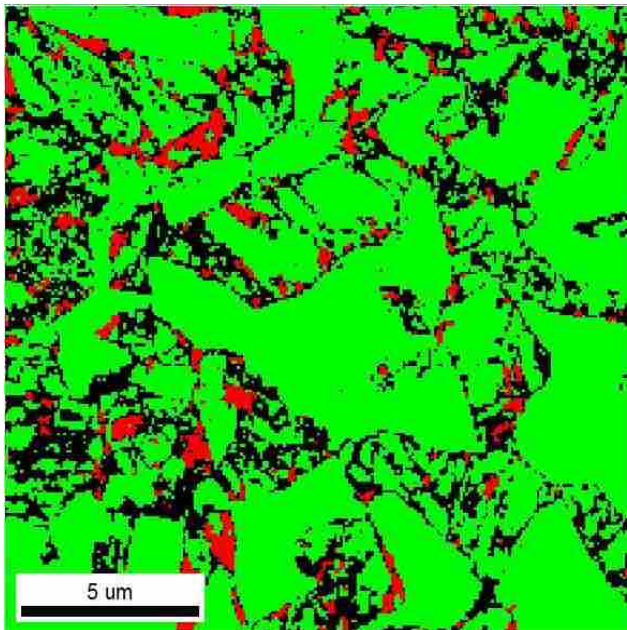

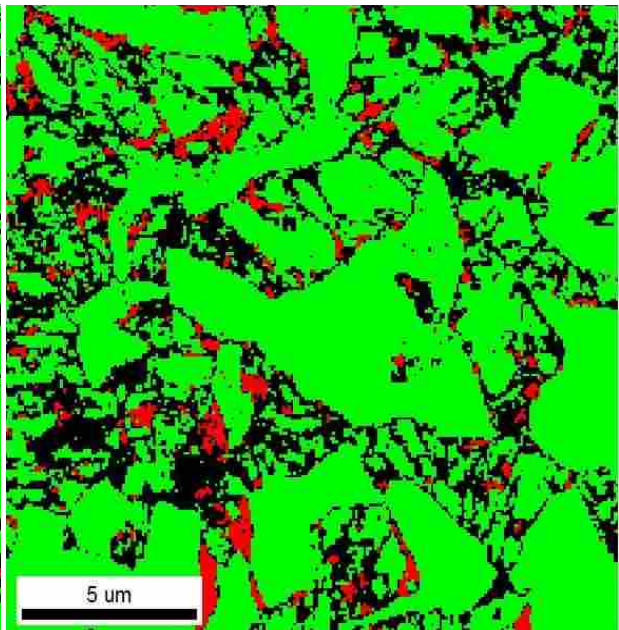Figure 27-Phase Map at 0% Strain
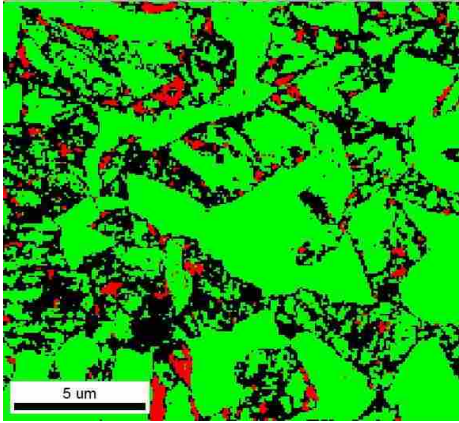

Figure 28-Phase Map at 2% Strain
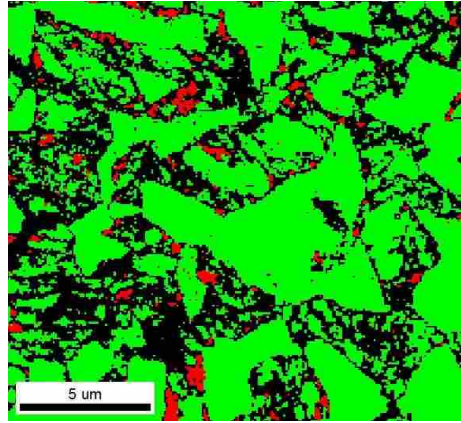
Figure 29-Phase Map at 4% Strain
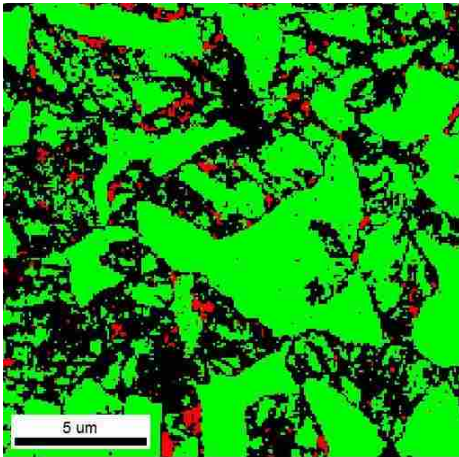

Figure 30-Phase Map at 6% Strain

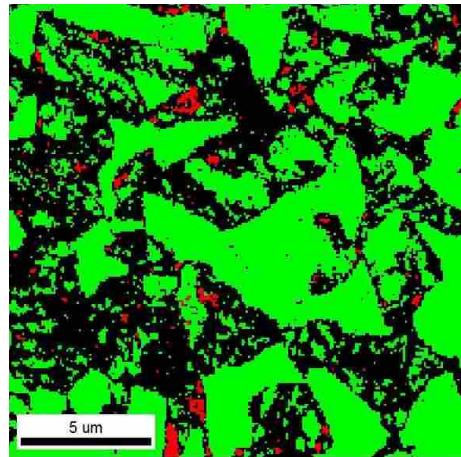Figure 31-Phase Map at 8% Strain

Figure 32-Phase Map at 10% Strain
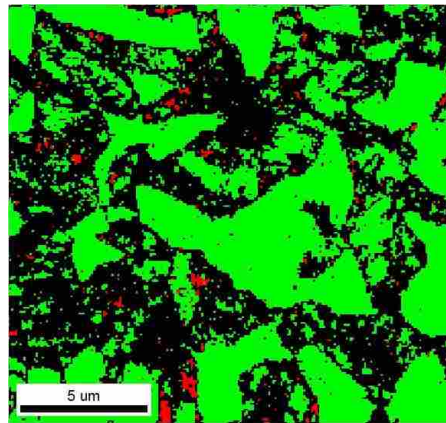
Figure 33-Phase Map at 12% Strain

The tests performed on the Instron test frame yielded the following stress/strain curve seen in Figure 34. Of interest is the degree to which the curve flattens before and after reaching it ultimate tensile strength of just under 1200Mpa. This is significant because it shows that the material undergoes a significant amount of uniform strain, and that the post-uniform strain is significant before true necking and ultimate failure.
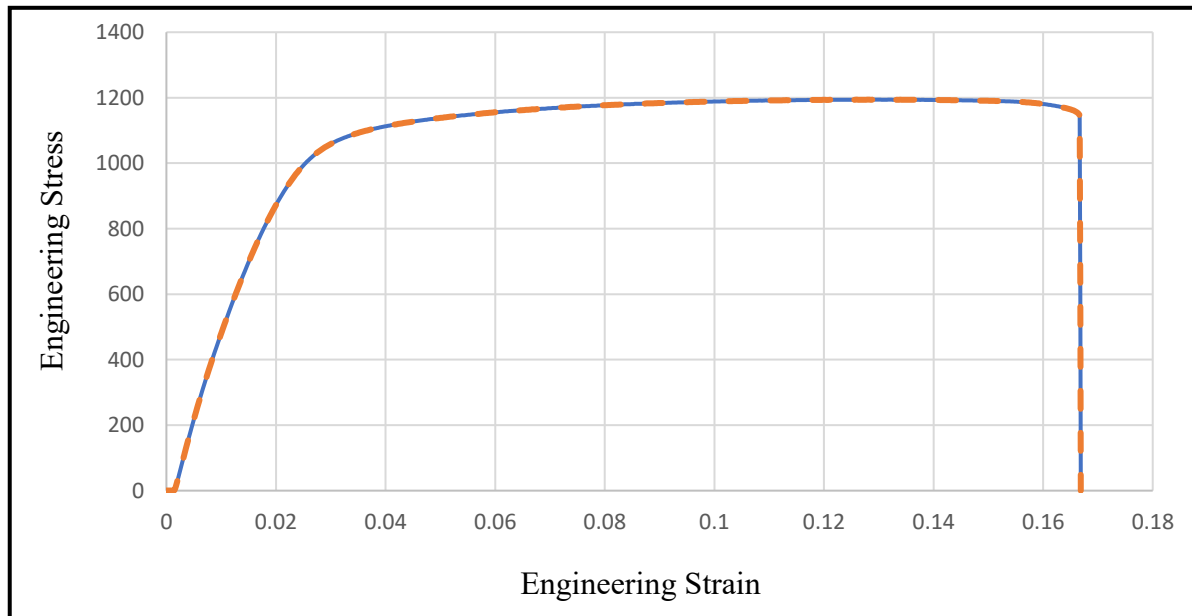
Figure 34-Tension Testing Results for 1mm Thick TBF1180

4.2 Forming Limit Diagram

The limit strain was determined by using the DIC software to calculate the strain rate at the eventual fracture site for each sample, where the samples were in true biaxial, plane and uniaxial tension followed by employing the following equation:

$$\dot{\varepsilon}_1(j) = \frac{d\varepsilon_1}{dt} \approx \frac{\varepsilon_1(j+1) - \varepsilon_1(j-1)}{2t} \tag{4-1}$$

Where $\dot{\varepsilon}_1$ is the strain rate in the major direction, ε_1 is the true strain in the major direction, τ is the period between frames and j is the frame number taken from the DIC analysis (Min, 2017). The value of τ in this study was approximately 1 second. Plots of this for each strain are found below. The point at which the strain rate begins to deviate from the line of best fit is considered the point of necking.
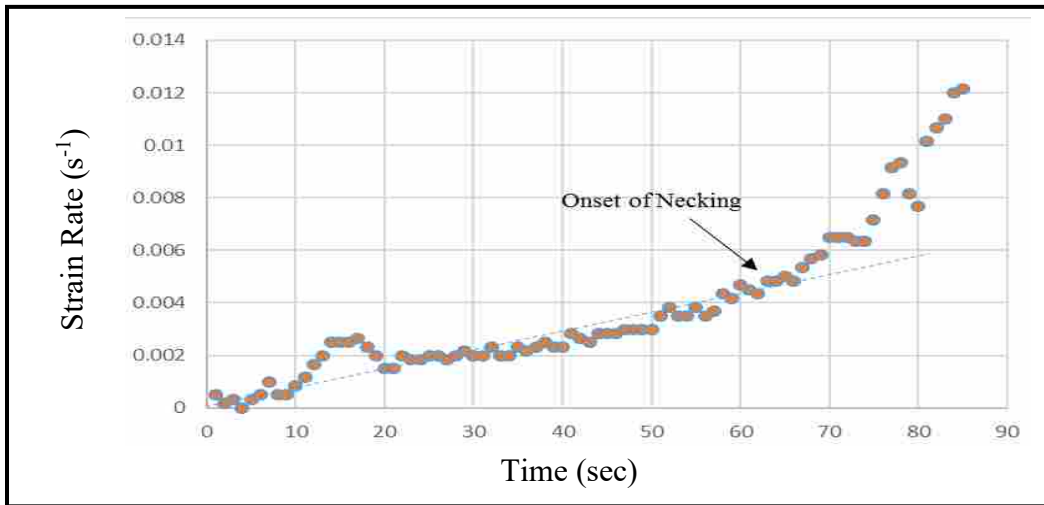
Figure 35-Strain Rate for Biaxial Tension to Identify Onset of Necking
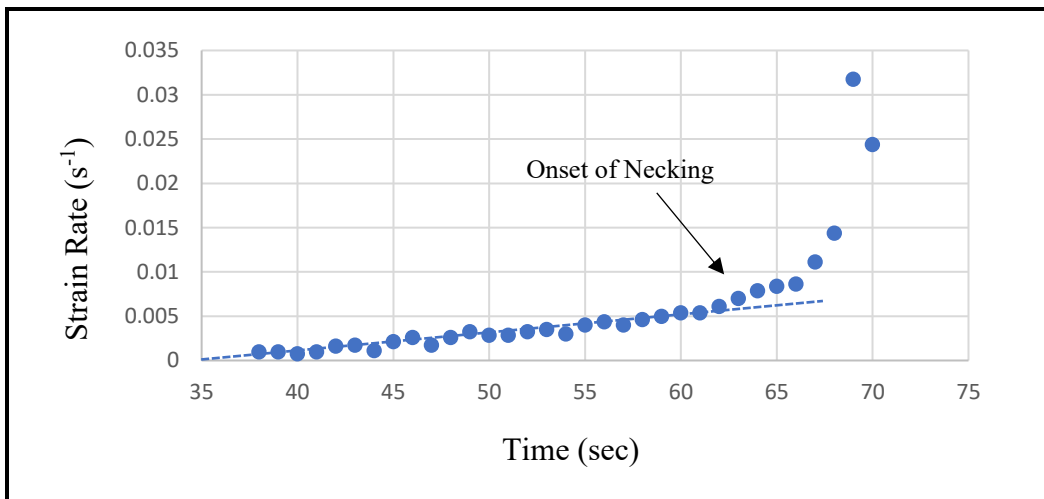
Figure 36-Strain Rate for Plane Tension to Identify Onset of Necking
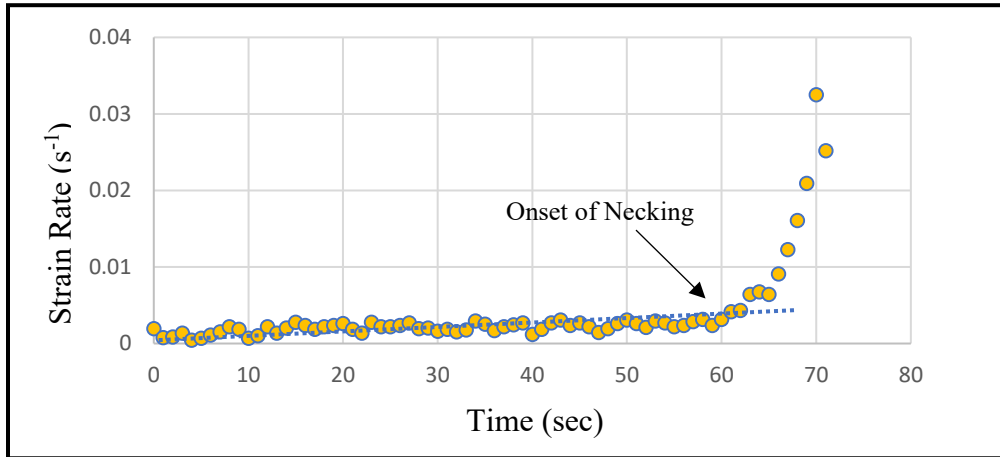
Figure 37-Strain Rate for Uniaxial Tension to Identify Onset of Necking

With the data in figures 35-37 above, the time at which necking occurred was obtained and used to determine the strain data at that point. The true major and minor strains for each strain path were then plotted in figure 38 below.
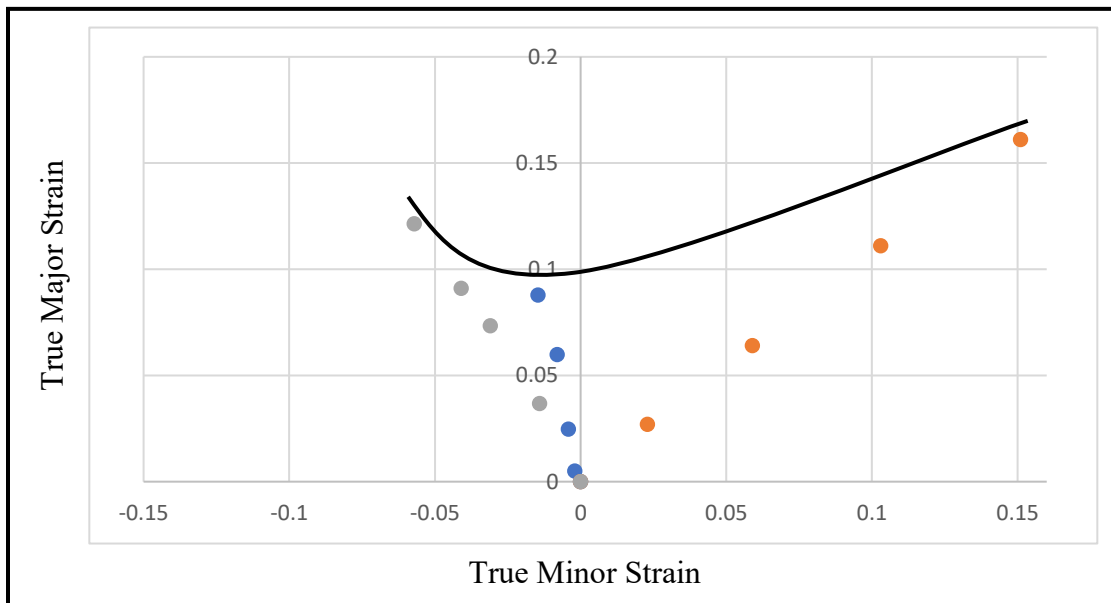
Figure 38-Forming Limit Diagram for TBF 1180 with Corresponding Strain Paths

The curve along the top of the points represents the forming limit, the point at which uniform elongation no longer occurs for a given strain path. As expected from historical behavior, the limit is notably higher for the biaxial and uniaxial paths than it is for the plane strain path.

4.3   Comparison with Q&P 1180

Both TBF 1180 and Q&P 1180 are similar in that they both have retained austenite and the same UTS but have a different microstructure that seems to affect formability. One of the main differences is the morphology of austenite, with TBF phases being smaller and thinner than the Q&P phases, which are larger and blocky. Phase maps of scans at 0% strain for both materials can been seen below in figures 39 and 40 (Cramer, 2017). Both images were taken at the same magnification with the same scan and step size.
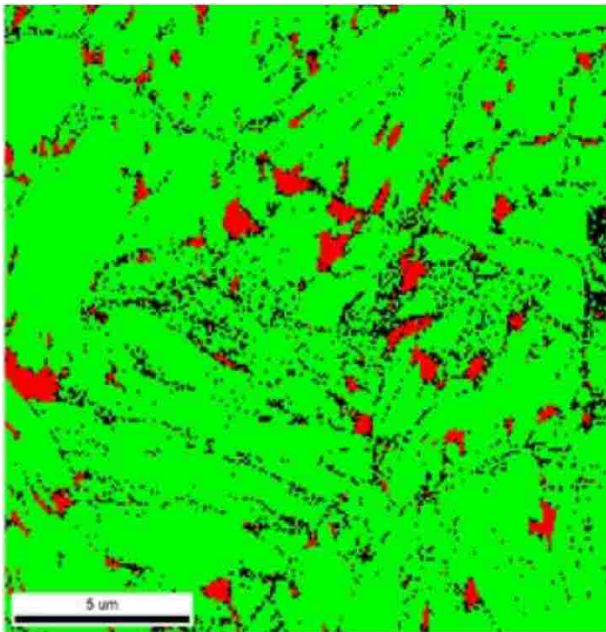
Figure 39-Phase Map of Q&P 1180   Figure 40-Phase Map of TBF 1180
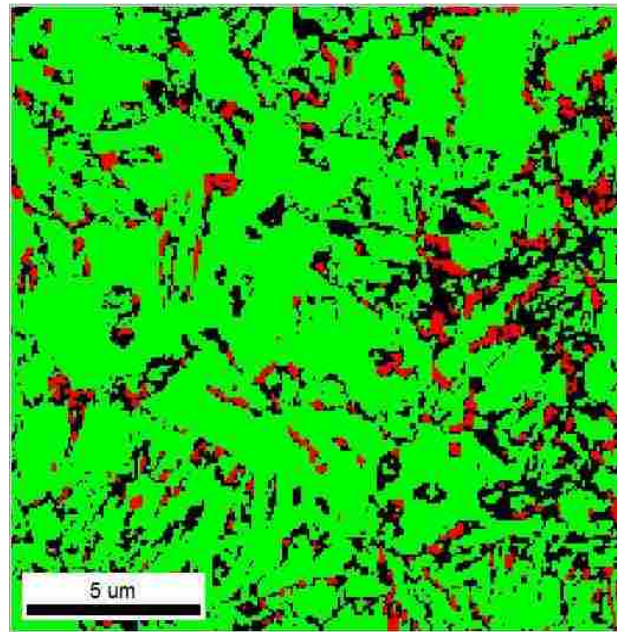
The significance of this difference is that TBF is potentially much more sensitive to the strain direction with respect to the austenite grain orientation. While the Q&P samples have grains that are relatively the same in any orientation, the TBF has a random mix of orientations for the longer and thinner grains. This could potentially explain the different conclusion reached in the 2017 Cramer paper in which uniaxial tension quickly depleted the retained austenite with minimal transformation after the first strain increment as observed in figure 41 below (Cramer, 2017).
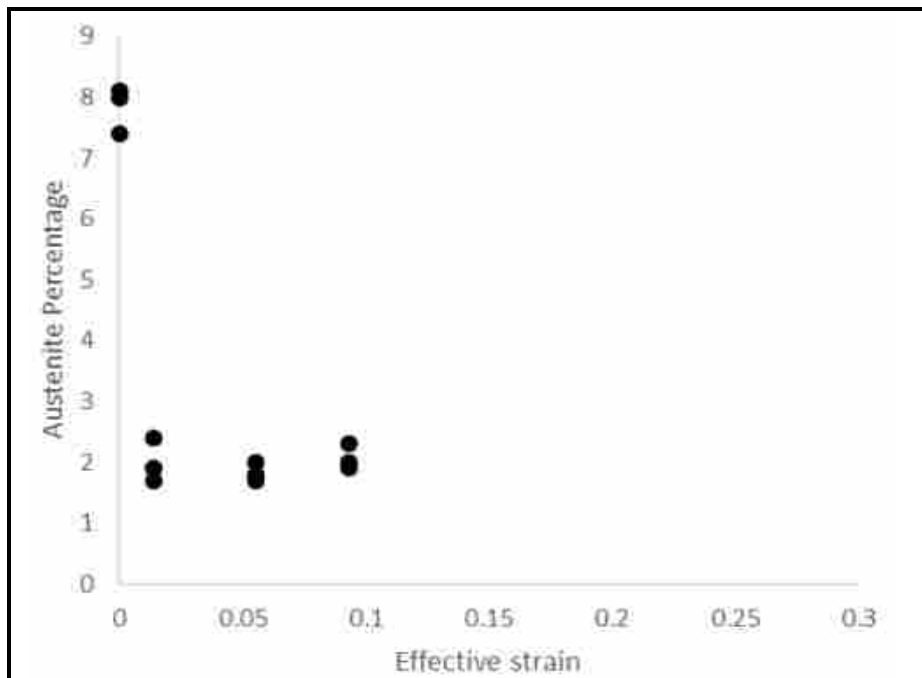
Figure 41-Percent RA as a Function of Effective Strain for Uniaxial Tension in Q&P 1180

Another comparison that can be made is between the total elongations of the two steels. In simple uniaxial tension tests, it can be observed that although approximately the same UTS is reached, the TBF exhibits a greater failure strain of about 0.165 while the Q&P sample reached only 0.15 as found in figure 42 (Cramer, 2017). The gradual slope of the Q&P curve could be attributed to the greater amount of RA reported which would allow for more gradual hardening

across the strain curve. Biaxial tests for both steels showed similar effective strains of 0.3 despite

the austenite levels being depleted quicker in the Q&P (Cramer, 2017).
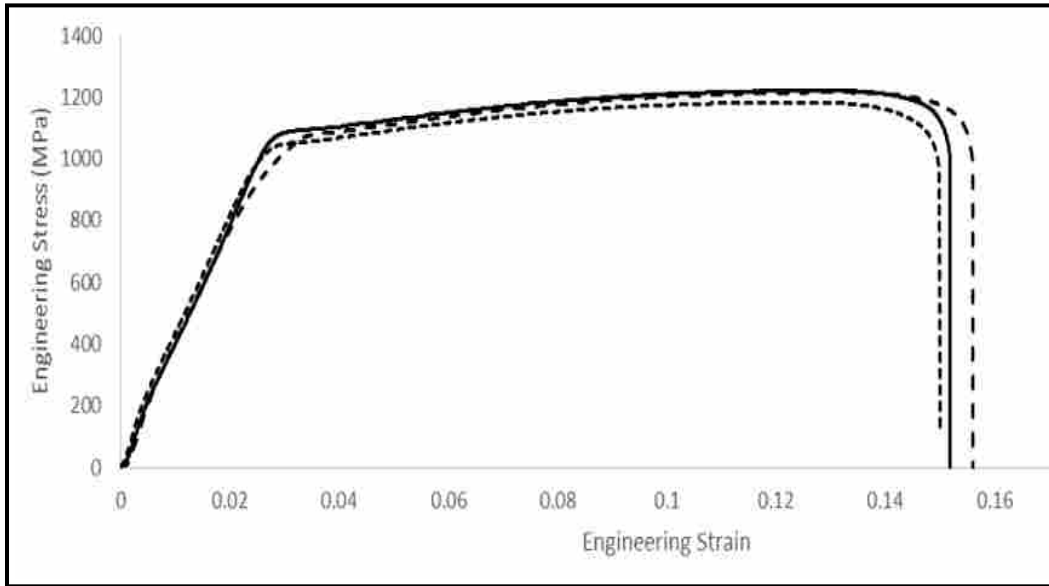
Figure 42-Tension Testing Results for 1.25mm Thick Q&P 1180
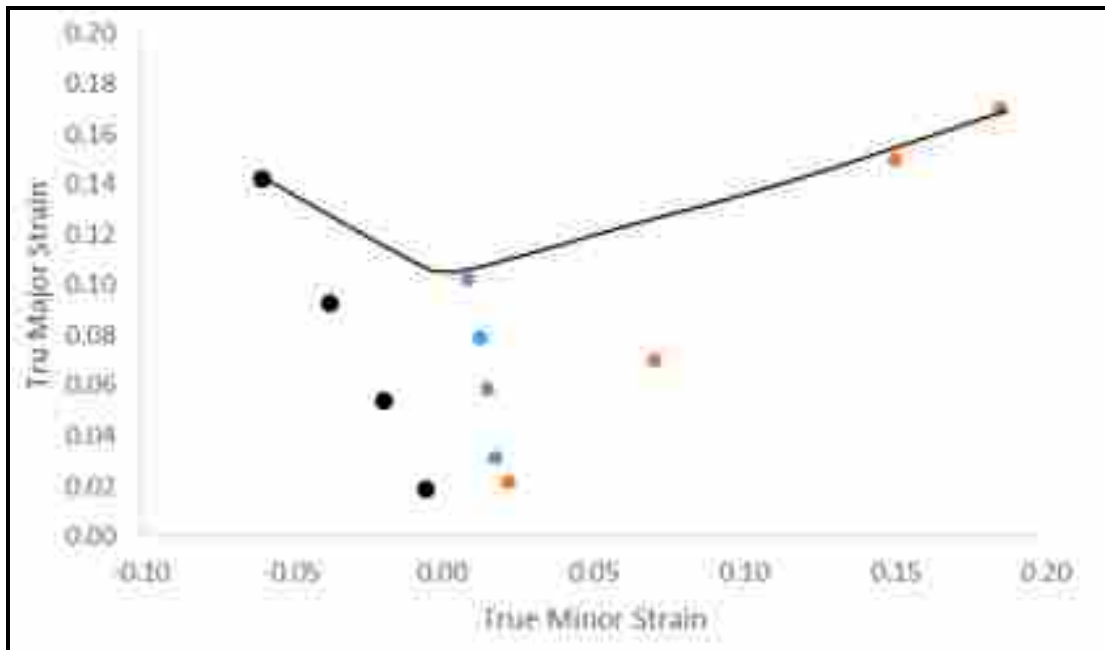
Figure 43-Forming Limit Diagram for Q&P 1180 with Corresponding Strain Paths

Of note are the differences between the forming limit diagrams of the materials. Although the shape of the limit curve is similar, the values are quite different found in figure 43 (Cramer, 2017). The Q&P exhibits slightly higher forming limits than the TBF for each strain path. However, TBF has more elongation after necking as evidenced by the stress/strain curves. Due to the flatness of the curve seen in figure 42, the post-uniform strain is still relatively uniform before a rapid failure. The Q&P stress/strain curve is similar to TBF but reaches its UTS later and exhibits less post-uniform strain before failure. The greater level of post-uniform strain in the TBF equates to greater practical formability, even if the strict definition of necking would seem to indicate less formability than the Q&P steel.

The last comparison to be made is the difference in initial retained austenite percentage. The Q&P is reported to have 7.5% RA as received while this study found only 5% RA as received in the TBF. The thermomechanical processing of the two steels, as well as the composition, are primarily responsible for the difference in initial RA content. But the polishing method is also a potential cause for the difference as it can cause premature RA transformation and can vary widely with the method used. Different grits of sandpaper and even the amount of pressure used when polishing introduce error from sample to sample. On the analysis side, the cleanup method used and whether the partition or total fraction was used will widely affect the RA percentage reported. This study used the total fraction of which takes the total RA amount and divides it by the total points in the scan while the Q&P study used the partition fraction which divides by the remaining points after cleanup. The total fraction reports a lower than accurate RA percentage because it is comparing it against unknown points that may or may not be ferrite. Using the partition fraction reports higher RA numbers but assumes that the missing points have an even distribution of austenite and ferrite. The result is that as scan quality degrades, reported RA percentage may rise

because only small amounts austenite transforms at high strains when points reported as ferrite decrease, thus the ratio of austenite to ferrite increases despite an overall decrease in austenite. Neither method is totally accurate although on high quality scans the difference in negligible. This is the main reason for better, standardized polishing techniques and alternative methods for determining RA content such as x-ray diffraction. Although the reported RA percentage may be reported low, the trend of austenite transformation observed in this study should remain consistent.

5   CONCLUSIONS

5.1   Summary of Work

The purpose of this research has been to study the effect of strain path on austenite transformation and formability in a 1mm thick TBF 1180 steel sheet.

The results of this study provide valuable information for all potential users of TBF 1180 including, but not limited to, auto manufacturers. It can be concluded that for all strain paths, austenite transformation does not have a linear relationship with effective strain. It was observed that the majority of austenite transformation occurred within the first 25% of its total effective strain to failure. The biaxial strain path exhibited the slowest rate of transformation, with approximately 2.6% austenite remaining at .05 effective strain. The uniaxial specimens averaged about 2.1% austenite while plane strain samples had roughly 1.2% at the same level of strain. At failure, the remaining austenite values for biaxial, uniaxial and plane were 1.1%, .9%, and .8% respectively.

The forming limits for TBF 1180 were very similar for biaxial and uniaxial strain paths, at about 0.12 true major strain, while plane strain samples necked sooner at about 0.075 true strain. This lines up reasonably well with the RA transformation rates of the different paths, where the plane strain path depleted RA quicker than the other paths.

Observation of the microstructure resulted in a confirmation that TBF steels form smaller, thinner grains of austenite, as opposed to the larger, block shaped grains found in the Q&P 1180.

The "formability" of TBF 1180 was found to be slightly worse than Q&P 1180, despite exhibiting more elongation prior to failure overall. The effect of strain path on austenite transformation was found to be different between the two steels with the uniaxial and plane strain paths essentially trading places. This is likely due in part to the different microstructures, where TBF appears to be more sensitive to RA grain orientation and strain direction. Unfortunately, a more thorough study is required to confirm this statement, where the grain morphologies and orientations need to be studied with respect to the transformation rate results.

Interestingly, the austenite transformation rate was significantly slower in biaxial tension than in plane tension which is the opposite result seen in Q&P 1180. This result will be studied with respect to microstructure details in future work.

5.2 Recommendations

Throughout the study, a few observations were made that could aid additional studies on this topic. Most notable would be further research and standardization of polishing methods to improve EBSD scan results and increase the accuracy of reported austenite percentage. The addition of x-ray diffraction to study the phase composition would likely shed light on the true as-received austenite percentage as well as increase the accuracy of RA percentage data.

A more thorough study of the microstructure would build upon the findings in this study. Possible studies could include strain direction with respect to the orientation of austenite grains. Furthermore, a deeper understanding of how neighboring grain properties affect RA transformation would help clarify the behavior of TBF while forming and could enhance the usability of the material.

REFERENCES

Basa, A., Thaulow, C., & Barnoush, A. (2014). Chemically Induced Phase Transformation in Austenite by Focused Ion Beam. Metallurgical and Materials Transactions A, 45(3), 1189-1198. doi:10.1007/s11661-013-2101-4

Bleck, W., et al. (1998). A comparative study of the forming-limit diagram models for sheet steels. *Journal of Materials Processing Technology* 83.1-3: 223-230.

Blondé, R., Jimenez-Melero, E., Zhao, L., Wright, J. P., Brück, E., van der Zwaag, S., & van Dijk, N. H. (2012). High-energy X-ray diffraction study on the temperature-dependent mechanical stability of retained austenite in low-alloyed TRIP steels. Acta Materialia, 60(2), 565-577. doi:https://doi.org/10.1016/j.actamat.2011.10.019

Choi, K. S., Liu, W. N., Sun, X., Khaleel, M. A., & Fekete, J. (2009). Influence of manufacturing processes and microstructures on the performance and manufacturability of advanced high strength steels. Journal of Engineering Materials and Technology, 131(4), 041205.

Cramer, J. (2017) "Strain Path Effect on Austenite Transformation and Ductility in Q&P 1180 steel." Thesis. Brigham Young University, Provo., BYU ScholarsArchive.

Di Gioacchino, F., & da Fonseca, J. Q. (2013). Plastic strain mapping with sub-micron resolution using digital image correlation. Experimental Mechanics, 53(5), 743-754.

Grajcar, A., Kuziak, R., & Zalecki, W. (2012). Third generation of AHSS with increased fraction of retained austenite for the automotive industry. Archives of civil and mechanical engineering, 12(3), 334-341.

Hausmann, K., D. Krizan, A. Pichler, and E. Werner (2013). Trip-aided bainitic-ferritic sheet steel: a critical assessment of alloy design and heat treatment. *MS&T'13*: 209-218.

Hausmann, K., et al. (2013). The influence of Nb on transformation behavior and mechanical properties of TRIP-assisted bainitic–ferritic sheet steels. *Materials Science and Engineering: A*588: 142-150.

Kuziak, R., Kawalla, R., & Waengler, S. (2008). Advanced high strength steels for automotive industry. Archives of civil and mechanical engineering, 8(2), 103-117. doi:http://dx.doi.org/10.1016/S1644-9665(12)60197-6

Kwon, O., Lee, K. Y., Kim, G. S., & Chin, K. G. (2010). New trends in advanced high strength steel developments for automotive application. Paper presented at the Materials Science Forum.

Min, J., Stoughton, T. B., Carsley, J. E., & Lin, J. (2017). Comparison of DIC Methods of Determining Forming Limit Strains. Procedia Manufacturing, 7(Supplement C), 668- 674. doi:https://doi.org/10.1016/j.promfg.2016.12.099

Moshksar, M. M., and S. Mansorzadeh (2003) Determination of the forming limit diagram for Al 3105 sheet. *Journal of Materials Processing Technology* 141.1: 138-142.

Shaw, J. R., & Zuidema, B. K. (2001). New High Strength Steels Help Automakers Reach Future Goals for Safety, Affordability, Fuel Efficiency and Environmental Responsibility. http://doi.org/10.4271/2001-01-3041

Sugimoto, K-I, et al. (2006). Formability of Nb bearing ultra high-strength TRIP-aided sheet steels. *Journal of Materials Processing Technology* 177.1-3: 390-395.

Sugimoto, K-I, et al. (2007). Formability of C–Si–Mn–Al–Nb–Mo ultra high-strength TRIP-aided sheet steels. *ISIJ international*47.9: 1357-1362.

Sugimoto, K-I. (2009). Fracture strength and toughness of ultra high strength TRIP aided steels. *Materials Science and Technology* 25.9: 1108-1117.

Systems, T. O. T. (2011). "Aramis 3D Digital Image Correlation Strain & 3D Deformation,".

Turrentine, T., Kurani, K. (2007). Car buyers and fuel economy?. *Energy policy* 35.2 (2007): 1213-1223.